



# Rod-shaped hydroxyapatite with mesoporous structure as drug carriers for proteins

Wandong Zhang<sup>a,\*</sup>, Yamin Chai<sup>a</sup>, Xianghua Xu<sup>a</sup>, Yonglan Wang<sup>b</sup>, Nana Cao<sup>a</sup>

<sup>a</sup> Department of Chemistry, School of Science, Tianjin University, and Collaborative Innovation Center of Chemical Science and Engineering (Tianjin), Tianjin 300072, China

<sup>b</sup> Stomatological Hospital, Tianjin Medical University, Tianjin 300070, China



## ARTICLE INFO

### Article history:

Received 15 May 2014

Received in revised form 8 October 2014

Accepted 14 October 2014

Available online 27 October 2014

### Keywords:

Hydroxyapatite

Mesoporous

Proteins

Drug delivery

## ABSTRACT

Rod-shaped hydroxyapatite (HAp) with mesoporous structure was synthesized by a hydrothermal method using Pluronic block co-polymer F127 as the template. The rod-shaped HAp was then tested as protein drug carriers by investigating their protein adsorption/release properties. Bovine serum albumin (BSA) and lysozyme (LSZ) were used as the model drugs. Various instrumental methods were used to characterize the structure, morphology, texture and protein drug adsorption/release properties of the samples. The amounts of BSA or LSZ adsorbed onto the rod-shaped HAp and their release profiles were evaluated in a simulated body fluid (SBF). The synthesized rod-shaped HAp had irregular mesostructures with lengths of 75–125 nm and diameters of about 25 nm. The rod-shaped HAp exhibited a higher loading capacity for BSA than for LSZ in the SBF. This adsorption behavior can be explained by the morphology of the rod-shaped HAp, which grew along the *c*-axis, leading to an *a*(*b*)-plane area that is larger than the *c*-plane area. Consequently, the number of positive charges on the surface of the rod-shaped HAp increased relative to the number of negative charges. The BSA release rate in SBF was slower than that of LSZ which is a result of the HAp surface properties.

© 2014 Elsevier B.V. All rights reserved.

## 1. Introduction

In recent years, there has been increasing interest in hydroxyapatite ( $\text{Ca}_{10}(\text{PO}_4)_6(\text{OH})_2$ , HAp) due to its nontoxicity, excellent biocompatibility and bioactivity [1]. It has been widely used as carriers in drug storage/release systems for various drugs [2–6]. Many chemical techniques have been employed to synthesize HAp crystals including sol-gel [7–9], hydrothermal [5,10,11], microemulsion [12], co-precipitation [4] and template-directed [13–15] methods.

Chemically synthesized HAp particles can have different morphologies such as spheres, needles, rods, fibers and plates. Recently, several researchers have prepared HAp particles with needle or rod morphologies [16]. These are of interest because HAp with needle-and rod-like shapes is the “building blocks” of teeth and bones in human calcified tissues, and also it is preferred for biomedical applications [17]. Rod-shaped HAp crystals have also been studied as carriers of protein drugs. Swain and Sarkar [18] showed that rod-shaped HAp exhibit higher bovine serum albumin (BSA) adsorption

capacity than spherical and fibroid HAp nanoparticles. A similar study was performed by Kawachi et al. [19]. They reported that rod-shaped HAp crystals with a large *a*-plane area had higher BSA adsorption than isotropic HAp.

In addition, mesoporous HAp has been used as carriers in drug adsorption/release systems, due to its large surface area and pore volume, which make it possible to carry high dosages of drugs into the mesopores [20]. Wu et al. [21] reported that mesoporous HAp particles synthesized with cetyltrimethyl ammonium bromide exhibited the highest BSA loading and the slowest release rate which was due to their high specific surface areas and small pore sizes. So the drug loading/release properties of drug carriers are affected by the particle morphologies, chemical composition and textural properties, such as surface area, pore volume and pore size.

However, protein adsorption/release characteristics are also related to the properties of the protein in the adsorption/release media [22]. To the best of our knowledge, there are no detailed reports about the adsorption/release behavior of acidic and alkaline proteins on mesoporous rod-shaped HAp. Particularly, the rod-shaped HAp particles show positive charge on its surface when suspended in simulated body fluid (SBF). Therefore, the adsorption/release properties of different proteins on mesoporous rod-shaped HAp needs to be evaluated.

\* Corresponding author. Tel.: +86 22 27403475; fax: +86 22 27403475.

E-mail address: [zhangwandong@tju.edu.cn](mailto:zhangwandong@tju.edu.cn) (W. Zhang).

In this study, mesoporous rod-shaped HAp was synthesized by a hydrothermal method using Pluronic block co-polymer F127 as the template. BSA and lysozyme (LSZ) were then chosen as the models for investigating the *in vitro* adsorption/release behavior of these proteins on the synthesized HAp. The amounts of BSA or LSZ adsorbed onto the rod-shaped HAp and their release profiles were evaluated in SBF.

## 2. Experimental

### 2.1. Chemicals and materials

Non-ionic surfactant Pluronic F127 (PVP, Mw 12,600) was purchased from Aladdin Chemical. Bovine serum albumin (assay min. 96%, PI 4.7, Mw 67,200 Da) and lysozyme (assay min. 80%, PI 11.2, Mw 14,600 Da) were purchased from Sigma Chemical. Other chemicals of analytical grade were purchased from domestic companies and used without further purification.

### 2.2. Synthesis and characterization of mesoporous rod-shaped HAp

Mesoporous rod-shaped HAp was prepared by a hydrothermal process. First 1.34 g of nonionic surfactant F127 was dissolved in 40 mL of 0.668 mol L<sup>-1</sup> (NH<sub>4</sub>)<sub>2</sub>HPO<sub>4</sub> solution with vigorous stirring at room temperature for 2 h. Then 40 mL of 1.120 mol L<sup>-1</sup> of Ca(NO<sub>3</sub>)<sub>2</sub>·4H<sub>2</sub>O solution was slowly added dropwise to the solution. During the precipitation process, the pH of the solution was kept at 10 by the addition of ammonia solution. After additional agitation for 20 min, the solution was transferred into a Teflon bottle (100 mL) and placed in a sealed stainless steel autoclave at 120 °C for 12 h. The autoclave was then allowed to cool to room temperature naturally and the precipitate was separated by centrifugation and then washed with deionized water repeatedly. The obtained products were dried in an oven at 100 °C for 24 h. The particles were then ground in an agate mortar for further characterization.

To investigate the phase composition and crystallinity of the synthesized HAp, X-ray diffraction (XRD) analysis was performed with a BDX 3300 diffractometer using a Cu K $\alpha$  radiation ( $\lambda=0.1542\text{ \AA}$ ), in the step scanning mode with a tube voltage of 30 kV and a tube current of 30 mA. The chemical and structural compositions of the samples were studied using a Bruker ALPHA-E Fourier transform infrared (FTIR) spectrometer in the frequency range of 4000–400 cm<sup>-1</sup>. The N<sub>2</sub> adsorption/desorption isotherms were measured using an Autosorb-Quantachrome NOVA 1200 surface area analyzer (Japan) at liquid nitrogen temperature (77 K). The mesoporous HAp samples were outgassed at 300 °C for 3 h prior to measurement. Specific surface areas were calculated by the Brunauer–Emmett–Teller (BET) method using the adsorption isotherms and pore size distributions were calculated by the Barrett–Joyner–Halenda (BJH) method using the desorption isotherms. Scanning electron microscopy (SEM, Hitachi 4800-S) was employed to characterize the morphological features of the HAp samples which were sputter-coated with gold prior to examination. An energy-dispersive X-ray (EDX) analyzer (Hiroba EDS) which was directly connected to the SEM instrument was used to investigate the chemical composition of the sample. Transmission electron microscopy (TEM) was used to observe the sizes and shapes of the HAp samples. Data were collected digitally using a JEM-2100F microscope with an accelerating voltage of 200 kV. The Ca/P ratios in the dried powders were measured by a chemical titration method.

**Table 1**  
Order, amounts and concentrations of reagents for preparing 1 L of SBF.

Order	Reagent	Amount (g)	Concentration (mmol L <sup>-1</sup> )
1	NaCl	6.540	112.00
2	NaHCO <sub>3</sub>	2.260	27.00
3	KCl	0.360	5.00
4	Na <sub>2</sub> HPO <sub>4</sub> ·2H <sub>2</sub> O	0.180	1.00
5	MgCl <sub>2</sub> ·6H <sub>2</sub> O	0.300	1.50
6	1.0 mol L <sup>-1</sup> HCl	≤3 mL	–
7	CaCl <sub>2</sub>	0.260	2.50
8	Na <sub>2</sub> SO <sub>4</sub>	0.060	0.50
9	Tris	6.060	50.00
10	1.0 mol L <sup>-1</sup> HCl	≤50 mL	–

### 2.3. Protein adsorption/release on the rod-shaped HAp

The procedure of drug loading and *in vitro* release was performed according to the method described in the literature [23]. BSA and lysozyme were used as model proteins in this study. The protein adsorption on HAp particles and release from that was investigated in simulated body fluid (SBF) (pH 7.40). Briefly, SBF was prepared by dissolving reagent grade NaCl, NaHCO<sub>3</sub>, KCl, Na<sub>2</sub>HPO<sub>4</sub>·2H<sub>2</sub>O, MgCl<sub>2</sub>·6H<sub>2</sub>O, CaCl<sub>2</sub>, Na<sub>2</sub>SO<sub>4</sub> and (CH<sub>2</sub>OH)<sub>3</sub>CNH<sub>2</sub> into deionized water, and buffering the mixture to pH 7.40 with hydrochloric acid. The detailed procedures to prepare SBF refer to Ref. [24]. The order, amounts and concentrations of reagents for preparing 1 L of SBF are given in Table 1.

In order to estimate the amount of protein adsorbed on the rod-shaped HAp, 20 mg of BSA or LSZ was added to 20 mL of SBF. The concentration of protein was measured by ultraviolet (UV) spectroscopy at 280 nm. Then 0.2 g of HAp was added and the solution was stirred at room temperature for 6 h. After being centrifuged, the proteins-loaded HAp was dried in air, and the concentrations of protein (BSA or LSZ) in the filtrate were measured by UV spectroscopy. The protein loading was calculated according to the difference between the initial and final protein concentrations [25]. A calibration curve was made for each set of measurements by plotting the absorbance vs. the protein concentration. Protein concentrations were between 0 and 1.0 mg mL<sup>-1</sup> and the correlation coefficient of the line was  $R^2 = 0.9999$ .

For the desorption experiments, the dried BSA-loaded HAp or LSZ-loaded HAp samples (0.20 g) were immersed in 20 mL of SBF at pH 7.4 and agitated in a horizontally shaking water bath at 37 °C. At predetermined time intervals, the solution was centrifuged, and then the release solution was withdrawn and replaced with fresh SBF solution (4.0 mL). The amount of the protein released was also determined by UV spectroscopy.

The weight loss and thermal stability of the loaded samples were evaluated using thermogravimetric (TG) analysis. A thermogravimetric/differential-scanning calorimetry (TG-DSC) study was performed on a NETZSCH STA 449C thermal analyzer by heating the samples from room temperature to 800 °C under an air atmosphere at a heating rate of 10 °C min<sup>-1</sup>. The chemical and structural compositions of the pure proteins and the protein-loaded HAp were also studied by FTIR spectroscopy. Zeta potential of the HAp particles were carried out with a Malvern Nano-ZS Zetasizer, and SBF solution was used as the dispersant.

## 3. Results and discussion

### 3.1. Characterization of rod-shaped HAp

Fig. 1 shows the XRD patterns of the HAp powder synthesized by hydrothermal treatment at 120 °C for 12 h (Fig. 1A) and the standard data for hexagonal HAp (Fig. 1B). All the diffraction peaks of the synthesized sample are characteristic of the pure hexagonal

**Table 2**

The lattice parameters, crystallite size,  $d$  spacing and degree of crystallinity of the synthesized HAp.

Sample	Lattice parameter (nm)	$d$ Spacing (nm)	Crystallinity (%)	Crystallite size (nm)
Standard HAp*	$a_0$ 0.9418	$c_0$ 0.6884	(002) 0.3440	(002)
HAp	0.9415	0.6884	0.3436	90.4 33.6

\* Hydroxyapatite ICDD PDF # 9-432.

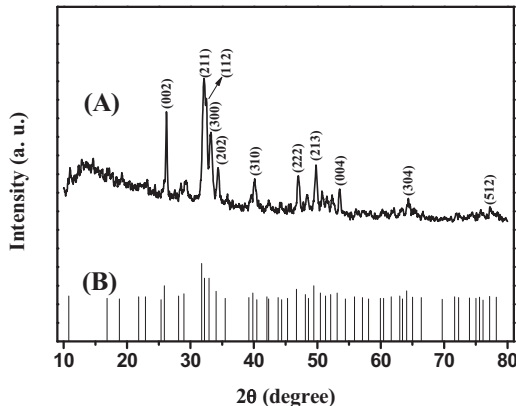


**Fig. 1.** XRD patterns of the mesoporous HAp particles (A) and standard HAp (B).

phase (JCPDS card No. 9-432). Therefore, the synthesized sample is phase-pure hydroxyapatite. There are no characteristic peaks for impurities in the spectrum, indicating that the surfactant did not influence the phase formation.

The XRD peaks can be used to estimate the crystallite size in the direction perpendicular to the crystallographic (002)-plane using Scherer's formula [26]. The lattice parameters, the  $d$  spacing and the crystallinity of the synthesized rod-shaped HAp from the (002) crystal face were obtained using MDI Jade 6.1 software [27,28]. This data are given in Table 2. The crystallinity of the HAp calculated from the integration of the XRD peaks was about 90.4%, indicating a relatively high crystallinity. The lattice parameters and  $d$  spacing value of the HAp sample are consistent with the data for pure hexagonal HAp (JCPDS No. 9-432). The crystallite size of the HAp synthesized with F127 was about 33.6 nm for the (002) crystal plane.

FTIR spectroscopy was carried out to study the chemical structure of the sample. Usually, there are four vibrational modes present for phosphate ions ( $\nu_1$ ,  $\nu_2$ ,  $\nu_3$  and  $\nu_4$ ) and two for carbonate ions ( $\nu_2$  and  $\nu_3$ ) [29]. Fig. 2 shows the FTIR spectra of the sample hydrothermally synthesized with the F127 template. The peak at

962 cm<sup>-1</sup> corresponds to non-degenerate symmetric stretching,  $\nu_1$ , of the P\O bond in the phosphate group [30], and the weak peak at 474 cm<sup>-1</sup> is the doubly degenerate phosphate bending mode,  $\nu_2$ . The peaks at 1033 and 1092 cm<sup>-1</sup> are ascribed to stretching vibration modes,  $\nu_3$ , of the PO<sub>4</sub><sup>3-</sup> group. The band between 564 and 603 cm<sup>-1</sup> belongs to the triply degenerate O\P\O bending mode,  $\nu_4$  [23]. Some researchers have reported that if HPO<sub>4</sub><sup>2-</sup> is present in the crystal lattice, then there are characteristic peaks at 1130 [31], 875 and 959 cm<sup>-1</sup> [32]. However, here there is no evidence that HPO<sub>4</sub><sup>2-</sup> is present, which indicates that the sample is not calcium-deficient HAp.

Carbonate ions can substitute for either OH<sup>-</sup> or PO<sub>4</sub><sup>3-</sup> ions in the apatite structure. The peak at 876 cm<sup>-1</sup> indicates a  $\nu_2$  bending mode of CO<sub>3</sub><sup>2-</sup> groups and suggests a B-type carbonate substitution, i.e., CO<sub>3</sub><sup>2-</sup> for PO<sub>4</sub><sup>3-</sup> [33]. The  $\nu_3$  stretching mode of CO<sub>3</sub><sup>2-</sup> is also observed at 1417 and 1455 cm<sup>-1</sup>, which reveals that a certain level of carbonate substitution has taken place in the product. The carbonate ions probably originate from a reaction between atmospheric carbon dioxide and the solution during the synthesis process. It has been shown that carbonate-containing HAp has better bioactivity than pure HAp which is due to its similarity with human bone [34]. Therefore, the sample synthesized in this study is expected to possess good biocompatibility.

The peaks at 633 and 3572 cm<sup>-1</sup> corresponded to the vibrational mode and intramolecular stretching vibration of the HAp hydroxyl groups, respectively. The peak at 1635 cm<sup>-1</sup> is due to the bending mode of the hydroxyl group in the adsorbed water. Based on the above analyses, these OH<sup>-</sup> and PO<sub>4</sub><sup>3-</sup> bands can be assigned to crystalline calcium HAp, which again indicates that the HAp sample has good crystallinity. The FTIR results are in good agreement with the XRD results.

Figs. 3 and 4, respectively, show the SEM and TEM images of the HAp sample synthesized by hydrothermal treatment at 120 °C for 12 h. As shown in Figs. 3A and 4A, HAp has a cylindrical rod-like morphology, with diameters of about 25 nm and lengths between 75 and 125 nm. The particle sizes from the images are in good agreement with the sizes calculated from the XRD data (Table 2). The rod-shaped HAp with much small particle sizes prefers to aggregate together and form accumulated pores. From Fig. 4, we can see that the numerous individual mesopores (white nanodots) with an average size of 3–4 nm spread around the surfaces of rod-shaped HAp, indicating the mesoporous structure of the sample.

The corresponding EDS spectrum in Fig. 3B shows that the chemical elements in the HAp are mainly calcium, phosphorus and oxygen. The average Ca/P molar ratio in the HAp is about 1.7, which is slightly higher than that in stoichiometric HAp (1.67). Meanwhile, the chemical titration results also reveal that the Ca/P molar ratio is 1.71. This implies that a small fraction of the PO<sub>4</sub><sup>3-</sup> in the HAp lattice was replaced by CO<sub>3</sub><sup>2-</sup> which is confirmed by the XRD and FTIR results. The XRD results do not show any crystalline carbonate salts and the FTIR spectrum contains bands at 1460 and 1420 cm<sup>-1</sup> which are assigned to the CO<sub>3</sub><sup>2-</sup> groups in B-type carbonated apatite.

The high-magnification TEM image (Fig. 4B) shows well-resolved lattice fringes which confirms that the synthesized sample is highly crystalline. The distance between the adjacent lattice fringes is 0.28 nm which is in good agreement with the  $d_{211}$  spacing value in the literature (0.2814 nm, JCPDS No. 9-432). So again, these

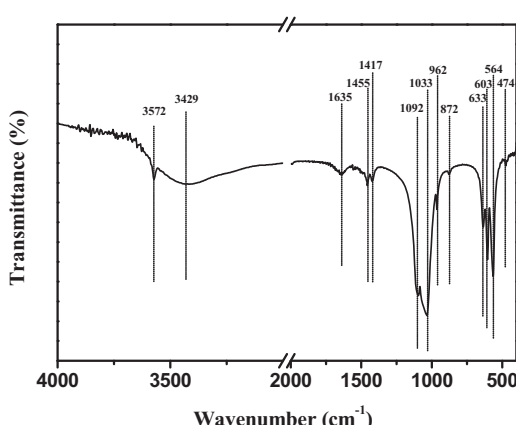


**Fig. 2.** FTIR spectra of the HAp particles.

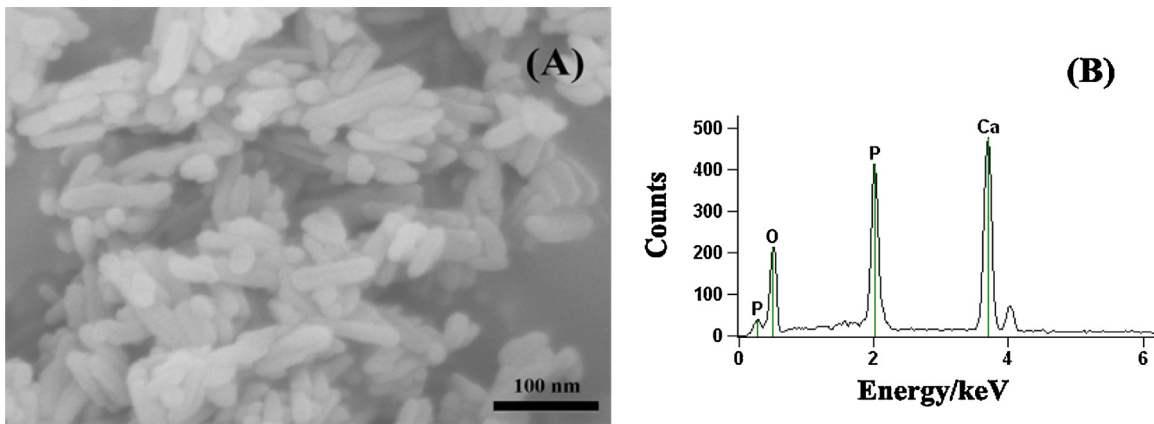


**Fig. 3.** (A) SEM image and (B) EDS spectrum of HAp synthesized by hydrothermal treatment at 120 °C for 12 h.

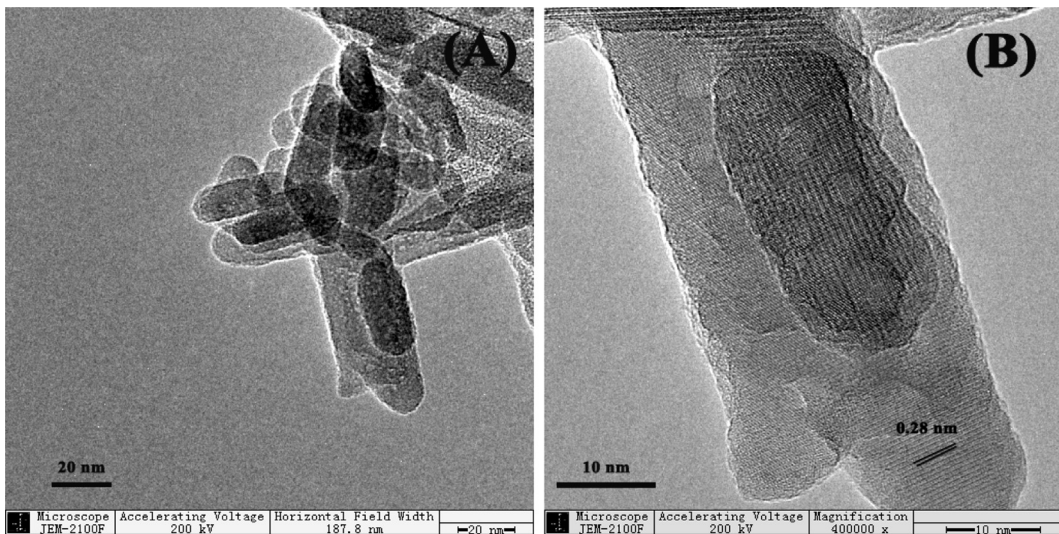


**Fig. 4.** TEM image of HAp. (A) Low-magnification image; (B) high-magnification image.

results indicate that the synthesized sample is well-crystallized with a typical apatite structure.

The N<sub>2</sub> adsorption/desorption isotherm and pore size distribution of the synthesized rod-shaped HAp are shown in Fig. 5.

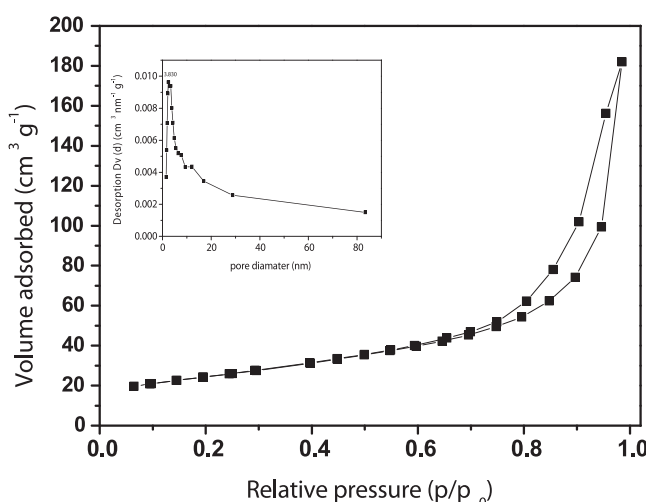


**Fig. 5.** The N<sub>2</sub> adsorption/desorption isotherms of the synthesized HAp sample. (The inset shows the pore size distributions.)

According to the International Union of Pure and Applied Chemistry classification system, the HAp particles exhibit a type IV isotherm with a distinct hysteresis loop. This demonstrates that the sample is a typical mesoporous material. The hysteresis between the adsorption and desorption curves is because the adsorption and desorption processes are irreversible [35].

Table 3 shows the pore diameter ( $D_p$ ), specific area ( $S_{BET}$ ) and pore volume ( $V_p$ ) for the HAp sample synthesized using F127 as a template. The HAp has a surface area of  $86.29 \text{ m}^2 \text{ g}^{-1}$  and a pore volume of  $0.27 \text{ cm}^3 \text{ g}^{-1}$ . The BJH method was used to calculate the pores size distribution using the desorption branch of the N<sub>2</sub> adsorption-desorption isotherm. The  $dV/dw$  pore volume vs. pore diameter curve (inset of Fig. 5) clearly shows a trimodal (about 3.83, 8.20 and 12.80 nm) distribution of pores, which mainly distributed around 3.83 nm. The smaller sized mesopores (i.e. the internal pores) in the HAp particles can be attributed to the removal of the F127 template. These results are in good agreement with the TEM analysis. The larger-sized pores (i.e. 8.20 and 12.80 nm) can be attributed to the aggregation of particles, as revealed by SEM image in Fig. 3.

**Table 3**  
N<sub>2</sub> adsorption/desorption parameters of the synthesized HAp.

sample	$S_{BET}$ ( $\text{m}^2 \text{ g}^{-1}$ )	$V_p$ ( $\text{cm}^3 \text{ g}^{-1}$ )	$D_p$ (nm)
HAp	86.29	0.27	Mainly 3.83

**Table 4**

The loading amount of BSA and LSZ after 6 h of immersion in SBF.

	BSA ( $\text{mg g}^{-1}$ )	LSZ ( $\text{mg g}^{-1}$ )
UV results	98.15	55.08
TG results	96.00	55.00

### 3.2. Comparison of BSA and LSZ adsorption/release behavior on the rod-shaped HAp

Previously, the adsorption kinetics of a variety of proteins on HAp or other biomaterials has been widely investigated [18,22,36–39]. These results showed that the adsorption of proteins onto HAp surfaces followed a Langmuir behavior and involved the formation of a monolayer of proteins. This behavior indicates that the amount of adsorbed protein increases as the initial protein concentration increases.

Based on these results, the adsorption of BSA and LSZ molecules at a protein concentration of  $1.0 \text{ mg mL}^{-1}$  was investigated and the results are shown in Table 4. The amount of protein adsorbed onto the rod-shaped HAp surfaces is different for the two proteins. More BSA was loaded onto the HAp than LSZ. This is because the hydroxyapatite particles have two different kinds of surface binding sites (C and P sites) [3]. After the HAp particles are dispersed in SBF, the C sites become positively charged and will bind to the acidic groups (mainly  $-\text{COO}^-$ ) in proteins, whereas the P sites become negatively charged and will bind to basic groups (mainly  $-\text{NH}_3^+$ ). BSA is negatively charged at a pH of 7.4, so it adsorbs onto the positively charged HAp sites (i.e. C-sites). In contrast, LSZ is positively charged at a pH of 7.4 and so it adsorbs onto the negatively charged sites (i.e. P-sites) [40]. So it can be concluded that the amount of adsorbed protein strongly depends on the charge of the protein and the sample. This is to say that electrostatic attractions play an important role on protein adsorption on mesoporous rod-shaped HAp.

Zeta potential of the HAp particles were carried out with a Malvern Nano-ZS Zetasizer, and SBF solution was used as the dispersant. Each sample was measured repeatedly five times and their mean value was obtained. The zeta potential indicates the surface charge property of the HAp particles when suspended in SBF solution (pH 7.4). The zeta potentials of the rod-shaped HAp particles in SBF was slightly positively charged (about 1.95 mV), leading to a tiny net charge on the surface. After adsorption of BSA, the zeta potential of the HAp decreased (transformed from positive to negative value) from 1.95 to  $-5.62 \text{ mV}$ , while, for LSZ, the zeta potential increased (became more positive) from 1.95 to  $9.56 \text{ mV}$ . The results suggested that protein has adsorbed to the surface of the rod-HAp particles.

Another important factor affecting protein adsorption is the texture of the HAp particles. The synthesized rod-shaped HAp are oriented along the  $c$ -axis, which makes the  $a(b)$ -plane area larger than the  $c$ -plane area. This results in an increase in the positive charge on the surface of the HAp particles. Kawachi et al. [19] reported that rod-shaped HAp crystals with a large  $a$ -plane area had higher adsorption of BSA than isotropic HAp. The relationship between protein adsorption and particle morphology has been studied in detail by Kandori et al. [41]. They reported that the rod-shaped HAp directly affected the amount of adsorbed BSA, whereas it only slightly affected the amount of adsorbed LSZ. This behavior further supports the fact that the C sites are the adsorption sites for BSA.

The thermal behavior of the prepared HAp-BSA and HAp-LSZ samples were studied in detail in the range of  $30\text{--}800^\circ\text{C}$  and the results are illustrated in Fig. 6A and B, respectively. For both samples, the weight loss in the first stage (below  $150^\circ\text{C}$ ) is probably due to the evaporation of absorbed water, the second stage loss

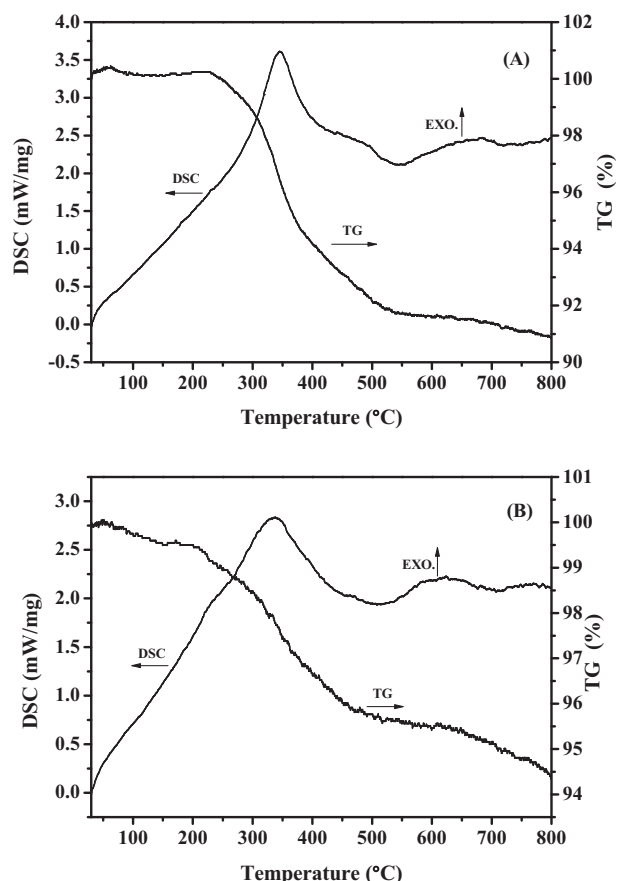
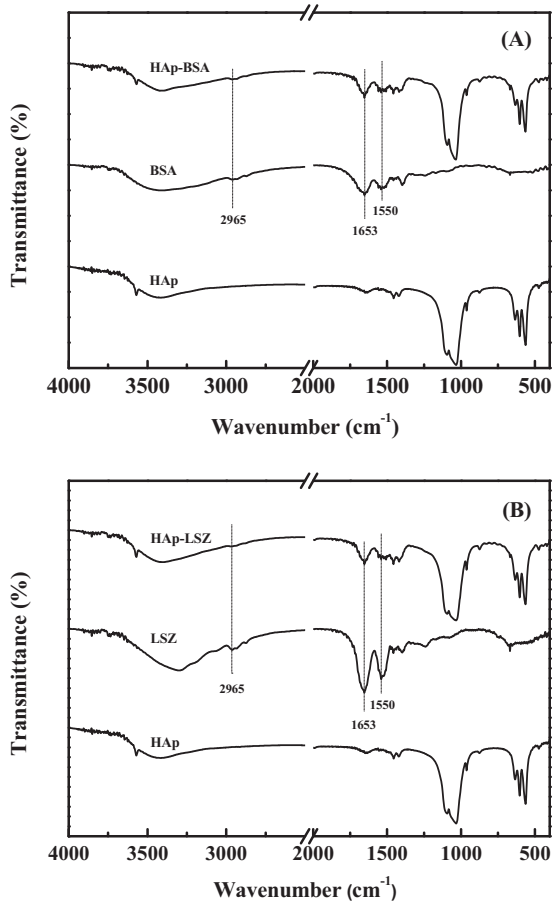


Fig. 6. The TG–DSC patterns of BSA-loaded HAp (A) and LSZ-loaded HAp (B) samples.

( $220\text{--}500^\circ\text{C}$ ) is probably due to the loss of the adsorbed protein (BSA or LSZ) as it is burned off, and the third stage loss ( $>700^\circ\text{C}$ ) is probably due to the loss of the constitution water in the HAp. The DSC curves for the two samples show exotherms in the range of  $200\text{--}400^\circ\text{C}$  which correspond to the burning off of the proteins. The total weight losses in BSA-HAp and LSZ-HAp were 9.0 and 5.5% between 30 and  $800^\circ\text{C}$ , respectively. This indicates that the amounts of absorbed BSA and LSZ in the final products are less than 9.0 and 5.5%, respectively. The amount of adsorbed protein as determined by the UV technique (shown in Table 4) is in good agreement with the TG results (within the error range), indicating that both methods are effective in determining the amount of adsorbed material.

Fig. 7 shows the FTIR spectra of the model drugs (BSA and LSZ), pure HAp and the drug-loaded HAp samples. Infrared spectra of proteins exhibit a number of amide bands due to different vibrations of the peptide moieties. The peak at  $1650 \text{ cm}^{-1}$  can be assigned to the amide I band which represents the stretching vibrations of the  $\text{C=O}$  bonds in the protein (Fig. 7A and B). The peak at  $1550 \text{ cm}^{-1}$  is due to the amide II band which represents the  $\text{C-N}$  stretch coupled with the  $\text{N-H}$  bending mode [42]. The bands at  $1650$  and  $1550 \text{ cm}^{-1}$  corresponding to BSA and LSZ, respectively, are also seen in the BSA-loaded HAp and LSZ-loaded HAp spectra. The peak at  $2965 \text{ cm}^{-1}$  represents  $-\text{CH}$  stretching in the pure proteins and the protein-loaded HAp. These results indicate that the rod-shaped HAp was successfully loaded with the proteins (BSA and LSZ). Swain and Sarkar [18] reported that the FTIR peaks of BSA adsorbed on HAp particles had the same characteristic wavenumber as those for pure BSA. This indicates that the BSA maintained its secondary structure when it was adsorbed. Zhu et al. [37] also reported that BSA will more or less alter its conformation and



**Fig. 7.** FTIR spectra of the pure HAp, BSA-loaded HAp and pure BSA (A); pure HAp, LSZ-loaded HAp and pure LSZ (B).

LSZ cannot change its conformation during adsorption on either hydrophilic or hydrophobic surface.

An in vitro release test was conducted by incubating the BSA- and LSZ-loaded HAp samples in SBF (pH 7.4) at 37 °C. The percentage of protein released from the carriers at various time intervals was determined by UV spectroscopy and the results are shown in Fig. 8A. The protein releasing trends for the BSA- and LSZ-loaded HAp samples are different. The BSA-loaded HAp exhibited a slow and sustained release of the protein, which is useful for prolonging drug release for up to 4 days. However, the LSZ-loaded HAp initially displays a burst-release phenomenon, i.e. over 50% of the loaded drugs are released in the first 7 h and then exhibited a slow release. The initial burst may be due to the loosely bound protein molecules being released from the surfaces of the HAp particles. The sustained release may be due to the release of the protein molecules from the accumulated pores as the SBF into the pores. The diffusion of the drug is the key factor which controls the release rate and this has been described in detail by Tomoda et al. [43].

Drug release kinetics from porous carrier materials is frequently described by the Higuchi model ( $Q = k * t^{1/2}$ , where  $Q$  is the amount of proteins released from HAp samples,  $t$  denotes release time and  $k$  is the release rate constant for the Higuchi model) [44,45]. Based on the model, fittings were presented in the Fig. 8B, it is clearly seen that both proteins display a two-step release and show fairly good fits to the original data.

It is known that mesoporous materials with high surface areas and pore volumes are ideal drug carriers for the adsorption of biologically active species [46]. The BSA molecules entered into the accumulated pores of the mesoporous rod-shaped HAp,

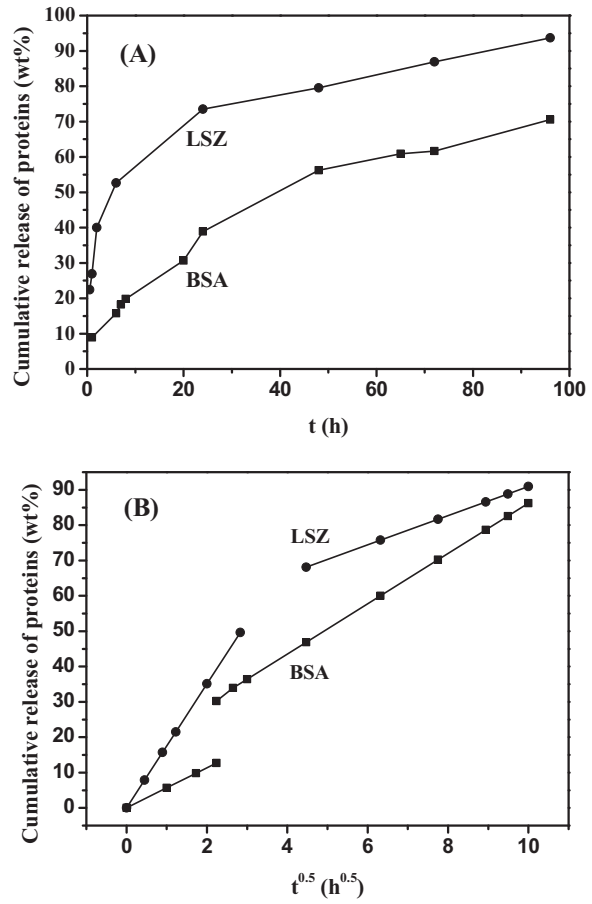


**Fig. 8.** (A) Release profiles of BSA and LSZ from the HAp samples in SBF at 37 °C and (B) the Higuchi plot for the release of proteins from HAp samples.

resulting in an increase in the adsorbed amount and a slow release of the protein. In addition, the HAp surface charge property is also an important factor to determining the adsorbed amount and release behavior of the proteins. According to the zeta potential tests, the higher electrostatic attractive forces between the positively charged HAp particles and the negatively charged BSA would enhance the adsorbed amount of BSA on the surface. This not only avoids a burst release of the protein but also prolongs the drug effect. All the results indicate that the mesoporous rod-shaped HAp show a favorable sustained release property for acidic proteins in drug-delivery systems.

#### 4. Conclusions

Mesoporous rod-shaped HAp was prepared with a hydrothermal method using F127 as the template. Structural characterizations by FTIR and XRD confirmed that the synthesized rod-shaped HAp had a pure standard HAp crystal structure. SEM and TEM observations showed the HAp had a rod-shaped morphology, with rod lengths of 75–125 nm and diameters of about 25 nm. The adsorption/desorption isotherms showed that the synthesized HAp had a mesoporous structure. The specific surfaces area was  $86.29 \text{ m}^2 \text{ g}^{-1}$  and the average pore volume was  $0.27 \text{ cm}^3 \text{ g}^{-1}$ . HAp showed net positive charged when suspended in SBF (about 1.95 mV) through zeta potential measurement. The rod-shaped HAp exhibited a higher drug-loading capacity and better sustained drug release properties for the negatively charged BSA than for the positively charged LSZ. This is due to the rods morphology, mesoporous structure and its surface properties. These results suggest that

mesoporous rod-shaped HAp could be used in the field of protein delivery.

## References

- [1] Y.R. Cai, R.K. Tang, Calcium phosphate nanoparticles in biominerization and biomaterials, *J. Mater. Chem.* 18 (32) (2008) 3775–3787.
- [2] P. Sibilla, A. Sereni, G. Aguiari, M. Banzi, E. Manzati, C. Mischiati, L. Trombelli, L. del Senno, Effects of a hydroxyapatite based biomaterial on gene expression in osteoblast-like cells, *J. Dent. Res.* 85 (4) (2006) 354–358.
- [3] Y.M. Guo, X.M. Shi, Q.L. Fang, J. Zhang, H. Fang, W.L. Jia, G. Yang, L. Yang, Facile preparation of hydroxyapatite-chondroitin sulfate hybrid mesoporous micro-rods for controlled and sustained release of antitumor drugs, *Mater. Lett.* 125 (2014) 111–115.
- [4] M. Öner, U. Uysal, Synthesis of hydroxyapatite crystals using carboxymethyl inulin for use as a delivery of ibuprofen, *Mater. Sci. Eng. C* 33 (1) (2013) 482–489.
- [5] Q.F. Zhao, T.Y. Wang, J. Wang, L. Zheng, T.Y. Jiang, G. Cheng, S.L. Wang, Template-directed hydrothermal synthesis of hydroxyapatite as a drug delivery system for the poorly water-soluble drug carvedilol, *Appl. Surf. Sci.* 257 (23) (2011) 10126–10133.
- [6] F. Ye, H.F. Guo, H.J. Zhang, X.L. He, Polymeric micelle-templated synthesis of hydroxyapatite hollow nanoparticles for a drug delivery system, *Acta Biomater.* 6 (6) (2010) 2212–2218.
- [7] X.Y. Ye, S. Cai, G.H. Xu, Y. Dou, H.T. Hu, Synthesis of mesoporous hydroxyapatite thin films using F127 as templates for biomedical applications, *Mater. Lett.* 85 (2012) 64–67.
- [8] J. Gil-Albarova, M. Vila, J. Badiola-Vargas, S. Sanchez-Salcedo, A. Herrera, M. Vallet-Regi, In vivo osteointegration of three dimensional crosslinked gelatin coated hydroxyapatite foams, *Acta Biomater.* 8 (2012) 3777–3783.
- [9] W.D. Zhang, N.N. Cao, Y.M. Chai, X.H. Xu, Y.L. Wang, Synthesis of nanosize single crystal strontium hydroxyapatite via a simple sol-gel method, *Ceram. Int.* 40 (2014) 16061–16064.
- [10] R. Morsya, M. Elsayed, R. Krause-Rehberg, G. Dlubek, T. Elnimr, Positron annihilation spectroscopic study of hydrothermally synthesized fine nanoporous hydroxyapatite agglomerates, *J. Eur. Ceram. Soc.* 30 (9) (2010) 1897–1901.
- [11] W.D. Zhang, Y.M. Chai, N.N. Cao, Y.L. Wang, Synthesis and characterization of selenium substituted hydroxyapatite via a hydrothermal procedure, *Mater. Lett.* 134 (2014) 123–125.
- [12] C. García, C. García, C. Paucar, Controlling morphology of hydroxyapatite nanoparticles through hydrothermal microemulsion chemical synthesis, *Inorg. Chem. Commun.* 20 (2012) 90–92.
- [13] M. Vallet-Regi, Evolution of bioceramics within the field of biomaterials, *C. R. Chimie* 13 (2010) 174–185.
- [14] Y.J. Wang, S.H. Zhang, K. Wei, N.R. Zhao, J.D. Chen, X.D. Wang, Hydrothermal synthesis of hydroxyapatite nanopowders using cationic surfactant as a template, *Mater. Lett.* 60 (2006) 1484–1487.
- [15] B. Prélöt, T. Zemb, Calcium phosphate precipitation in catanionic templates, *Mater. Sci. Eng. C* 25 (5–8) (2005) 553–559.
- [16] S.V. Dorozhkin, M. Epple, Biological and medical significance of calcium phosphates, *Angew. Chem. Int. Ed.* 41 (17) (2002) 3130–3146.
- [17] W. Amer, K. Abdelouandi, H.R. Ramananarivo, M. Zahouily, A. Fihri, Y. Coppel, R.S. Varma, A. Solhy, Synthesis of mesoporous nano-hydroxyapatite by using zwitterions surfactant, *Mater. Lett.* 107 (2013) 189–193.
- [18] S.K. Swain, D. Sarkar, Study of BSA protein adsorption/release on hydroxyapatite nanoparticles, *Appl. Surf. Sci.* 286 (2013) 99–103.
- [19] G. Kawachi, S. Sasaki, K. Nakahara, E.H. Ishida, K. Ioku, Porous apatite carrier prepared by hydrothermal method, *Bioceramics* 18, PTS 1 and 2, Key Eng. Mater. 309–311 (2006) 935–938.
- [20] D. Arcos, M. Vallet-Regi, Bioceramics for drug delivery, *Acta Mater.* 61 (2012) 890–911.
- [21] X.D. Wu, X.F. Song, D.S. Li, J.G. Liu, P.B. Zhang, X.S. Chen, Preparation of mesoporous nano-hydroxyapatite using a surfactant template method for protein delivery, *J. Bionic Eng.* 9 (2) (2012) 224–233.
- [22] T. Matsumoto, M. Okazaki, M. Inoue, S. Yamaguchi, T. Kusunose, T. Toyonaga, Y. Hamada, J. Takahashi, Hydroxyapatite particles as a controlled release carrier of protein, *Biomaterials* 25 (17) (2004) 3807–3812.
- [23] Y.P. Guo, Y.B. Yao, Y.J. Guo, C.Q. Ning, Hydrothermal fabrication of mesoporous carbonated hydroxyapatite microspheres for a drug delivery system, *Microp. Mesop. Mater.* 155 (2012) 245–251.
- [24] A. Nouri, R. Castro, J.L. Santos, C. Fernandes, J. Rodrigues, H. Tomas, Calcium phosphate mediated gene delivery using simulated body fluid (SBF), *Int. J. Pharm.* 434 (2012) 199–208.
- [25] K.L. Lin, P.Y. Liu, L. Wei, Z.Y. Zou, W.B. Zhang, Y. Qian, Y.H. Shen, J. Chang, Strontium substituted hydroxyapatite porous microspheres: surfactant-free hydrothermal synthesis, enhanced biological response and sustained drug release, *Chem. Eng. J.* 222 (2013) 49–59.
- [26] A.L. Giraldo-Betancur, D.G. Espinosa-Arbelaez, A. del Real-López, B.M. Millan-Malo, E.M. Rivera-Muñoz, E. Gutierrez-Cortez, P. Pineda-Gómez, S. Jimenez-Sandoval, M.E. Rodriguez-Garcia, Comparison of physicochemical properties of bio and commercial hydroxyapatite, *Curr. Appl. Phys.* 13 (7) (2013) 1383–1390.
- [27] Y.X. Sun, H. Yang, D.L. Tao, Microemulsion process synthesis of lanthanide-doped hydroxyapatite nanoparticles under hydrothermal treatment, *Ceram. Int.* 37 (7) (2011) 2917–2920.
- [28] S. Kannan, A. Rebelo, J.M.F. Ferreira, Novel synthesis and structural characterization of fluorine and chlorine co-substituted hydroxyapatites, *J. Inorg. Biochem.* 100 (10) (2006) 1692–1697.
- [29] I. Rehman, W. Bonfield, Characterization of hydroxyapatite and carbonated apatite by photo acoustic FTIR spectroscopy, *J. Mater. Sci. Mater. Med.* 8 (1) (1997) 1–4.
- [30] F. Bakan, O. Laçın, H. Sarac, A novel low temperature sol-gel synthesis process for thermally stable nano crystalline hydroxyapatite, *Powder Technol.* 233 (2013) 295–302.
- [31] Y.P. Guo, Y.B. Yao, C.Q. Ning, Y.J. Guo, L.F. Chu, Fabrication of mesoporous carbonated hydroxyapatite microspheres by hydrothermal method, *Mater. Lett.* 65 (14) (2011) 2205–2208.
- [32] Y.C. Wang, A.H. Yao, W.H. Huang, D.P. Wang, J. Zhou, In situ fabrication of hollow hydroxyapatite microspheres by phosphate solution immersion, *J. Cryst. Growth* 327 (1) (2011) 245–250.
- [33] J.D. Chen, Y.J. Wang, X.F. Chen, L. Ren, C. Lai, W. He, Qing Zhang, A simple sol-gel technique for synthesis of nanostructured hydroxyapatite, tricalcium phosphate and biphasic powders, *Mater. Lett.* 65 (12) (2011) 1923–1926.
- [34] A. Śliśarczyk, Z. Paszkiewicz, C. Paluszakiewicz, FTIR and XRD evaluation of carbonated hydroxyapatite powders synthesized by wet methods, *J. Mol. Struct.* 744–747 (2005) 657–661.
- [35] G. Verma, K.C. Barick, N. Manoj, A.K. Sahu, P.A. Hassan, Rod-like micelle templated synthesis of porous hydroxyapatite, *Ceram. Int.* 39 (8) (2013) 8995–9002.
- [36] K. Kandori, S. Mizumoto, S. Toshima, M. Fukusumi, Y. Morisada, Effects of heat treatment of calcium hydroxyapatite particles on the protein adsorption behavior, *J. Phys. Chem. B* 113 (31) (2009) 11016–11022.
- [37] X.D. Zhu, H.S. Fan, C.Y. Zhao, J. Lu, T. Ikoma, J. Tanaka, X.D. Zhang, Competitive adsorption of bovine serum albumin and lysozyme on characterized calcium phosphates by polyacrylamide gel electrophoresis method, *J. Mater. Sci. Mater. Med.* 18 (11) (2007) 2243–2249.
- [38] Z. Zhuang, M. Aizawa, Protein adsorption on single-crystal hydroxyapatite particles with preferred orientation to a(b)- and c-axes, *J. Mater. Sci. Mater. Med.* 24 (5) (2013) 1211–1216.
- [39] M. Öner, E. Yetiz, E. Ay, U. Uysal, Ibuprofen release from porous hydroxyapatite tablets, *Ceram. Int.* 37 (7) (2011) 2117–2125.
- [40] G.S. Lee, J.H. Park, U.S. Shin, H.W. Kim, Direct deposited porous scaffolds of calcium phosphate cement with alginate for drug delivery and bone tissue engineering, *Acta Biomater.* 7 (8) (2011) 3178–3186.
- [41] K. Kandori, A. Fudo, T. Ishikawa, Study on the particle texture dependence of protein adsorption by using synthetic micrometer-sized calcium hydroxyapatite particles, *Colloid Surf. B Biointerf.* 24 (2) (2002) 145–153.
- [42] P.N. Naik, S.A. Chimatadar, S.T. Nandibewoor, Study on the interaction between antibacterial drug and bovine serum albumin: A spectroscopic approach, *Spectrosc. Acta Pt. A* 73 (5) (2009) 841–845.
- [43] K. Tomoda, H. Ariizumi, T. Nakaji, K. Makino, Hydroxyapatite particles as drug carriers for proteins, *Colloid Surf. B* 76 (1) (2010) 226–235.
- [44] C.Y. Yang, W. Guo, L.R. Cui, D. Xiang, K. Cai, H.M. Lin, F.Y. Qu, pH responsive controlled release system based on mesoporous bioglass materials capped with mineralized hydroxyapatite, *Mater. Sci. Eng. C* 36 (2014) 237–243.
- [45] J. Andersson, J. Rosenholm, S. Areva, M. Linden, Influences of material characteristics on ibuprofen drug loading and release profiles from ordered micro- and mesoporous silica matrices, *Chem. Mater.* 16 (2004) 4160–4167.
- [46] Y.J. Guo, Y.Y. Wang, T. Chen, Y.T. Wei, L.F. Chu, Y.P. Guo, Hollow carbonated hydroxyapatite microspheres with mesoporous structure: hydrothermal fabrication and drug delivery property, *Mater. Sci. Eng. C* 33 (6) (2013) 3166–3172.